Pharmaceutical Research, Vol. 24, No. 12, December 2007 (© 2007)
DOI: 10.1007/s11095-007-9391-4

Featured Article

An In Silico Transwell Device for the Study of Drug Transport and Drug–Drug Interactions

Lana X. Garmire,[1] David G. Garmire,[2] and C. Anthony Hunt[3,4]

Received April 1, 2007; accepted June 25, 2007; published online 17 August 2007

Purpose. Validate and exemplify a discrete, componentized, in silico, transwell device (ISTD) capable of mimicking the *in vitro* passive transport properties of compounds through cell monolayers. Verify its use for studying drug–drug interactions.

Methods. We used the synthetic modeling method. Specialized software components represented spatial and functional features including cell components, semi-porous tight junctions, and metabolizing enzymes. Mobile components represented drugs. Experiments were conducted and analyzed as done *in vitro*.

Results. Verification experiments provided data analogous to those in the literature. ISTD parameters were tuned to simulate and match *in vitro* urea transport data; the objects representing tight junction (effective radius of 6.66 Å) occupied 0.066% of the surface area. That ISTD was then tuned to simulate pH-dependent, *in vitro* alfentanil transport properties. The resulting ISTD predicted the passive transport properties of 14 additional compounds, individually and all together in one in silico experiment. The function of a two-site enzymatic component was cross-validated with a kinetic model and then experimentally validated against *in vitro* benzyloxyresorufin metabolism data. Those components were used to exemplify drug–drug interaction studies.

Conclusions. The ISTD is an example of a new class of simulation models capable of realistically representing complex drug transport and drug–drug interaction phenomena.

KEY WORDS: agent-based modeling; discrete event; drug transport; drug–drug interaction; emergent properties; simulation.

INTRODUCTION

The recently described in silico transwell system (1,2) is an example of a class of synthetic, discrete, componentized, computational models that are intended for refining and testing hypotheses about interacting mechanisms occurring during transport across cell barriers (3–5). A feature of this new class of models is that autonomous, in silico components, representing specific inter- and intracellular counterparts, can be assembled and disassembled within the analogue system's framework to mimic, for example, a tightly confluent cell monolayer in a Transwell™ device that is being used for drug transport studies. The consequences of interactions between in silico mobile and fixed components, controlled by known or hypothesized component-specific principles, can be measured and studied. The resulting data can be compared with *in vitro* data to refine in silico behaviors and help clarify posited, causal linkages that may underlie the transport phenomena under investigation. Research on this class of models is motivated by five broad expectations. (1) Experimentation with such models will help unravel the complex processes encountered, for example, when two or more drugs interact simultaneously with various inducible transporters and metabolic enzymes. (2) Future device components can be "educated," for example as in (6), to use the calculated physicochemical properties (PCPs) of new compounds to provide in silico experimental results from which acceptable permeability predictions are obtained. (3) With progress on 1 and 2, relative transport properties of sets of new compounds can be explored in advance of costly wet-lab experiments with the intent of eliminating from further consideration those with unacceptable properties. (4) Predicted *in vivo* absorption properties of new compounds in animals and humans, based on high throughput *in vitro* data, will become increasingly accurate. (5) In silico screening will save time

---

Electronic supplementary material The online version of this article (doi:10.1007/s11095-007-9391-4) contains supplementary material, which is available to authorized users.

[1] Graduate Group in Comparative Biochemistry, University of California, Berkeley, California, USA.

[2] The Berkeley Sensor and Actuator Center, UC Berkeley, Berkeley, California, USA.

[3] BioSystems Group and the UCSF/UCB Joint Graduate Group in Bioengineering, Department of Biopharmaceutical Sciences, University of California, 513 Parnassus Ave., S-926, San Francisco, California 94143-0446, USA.

[4] To whom correspondence should be addressed. (e-mail: a.hunt@ucsf.edu)

ABBREVIATIONS: CYP, a P450 enzyme; ISTD, in silico transwell device; MW, molecular weight; PCP, physicochemical properties; PRN, pseudorandom number; SM, supplementary material; TD, transwell device.

and reduce costs. What capabilities must in silico analogues of *in vitro* systems exhibit in order to realize these expectations? Their realization requires pushing modeling and simulation capabilities to an entirely new level. We specify nine capabilities in Appendix that the envisioned new class of models will need to exhibit to achieve the preceding expectations.

The feasibility of using synthetic models in this context was demonstrated by an earlier in silico transwell system (1,2). The in silico transwell device (ISTD) used for all studies and sketched in Fig. 1 is an improvement. The simulations rely on new mechanisms of component interaction. The goal of this project has been to verify and validate aspects of the ISTD. The results are evidence of an important step toward achieving the above expectations. The ISTD realistically simulates the 3D characteristics of a Transwell device containing a confluent cell monolayer. We introduce and validate a removable component that represents the semi-porous tight junctions between cells. Its mechanism draws on existing physical models of solute movement through tight junctions. A mechanism of passive transport is presented that simulates solute movement. Separate components represent the compounds of interest. Their movement and transport are governed by compound-specific logic. That logic relies primarily on local information and the PCPs of the compound (real or hypothetical) being simulated. Another component represents drug-metabolizing enzymes. It has two interacting substrate binding sites.

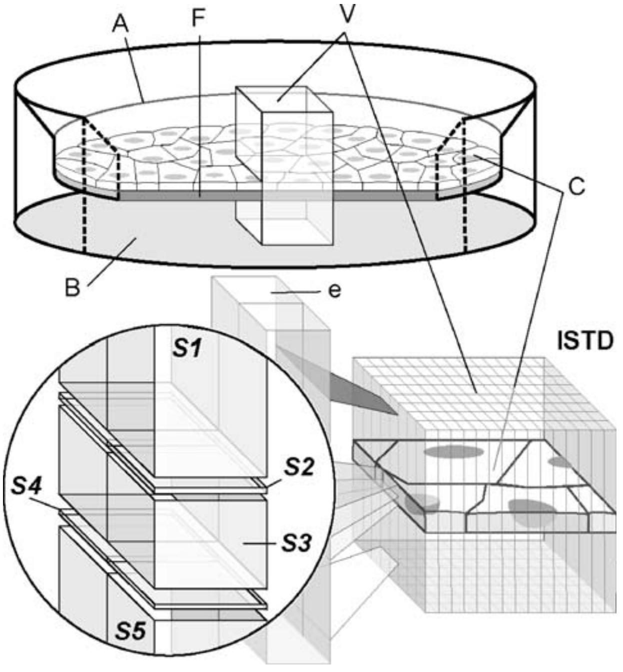

Fig. 1. Transwell devices: *in vitro* and in silico. *A* Apical compartment, *B* basolateral compartment, *C* epithelial cell (e.g., Caco-2) monolayer, *F* support filter, *V* an arbitrary vertical column section through the system. *ISTD* The in silico transwell device. *e* One of the 10,000 simulated 3D elements of S1. *Insert S1–S5 from top to bottom* These five simulated 3D spaces represent the apical compartment, apical cell membranes, intracellular spaces, basolateral cell membranes, and the basal compartment of the transwell device; their relative sizes are indicated; two elements in each space are shown.

Verification experiments using over a hundred different hypothetical compounds (see "Supplementary Material") show that their simulated passive transport properties are analogous to literature observations. An ISTD parameterization is presented, which validates against *in vitro* transport data for urea and alfentanil. Without further adjustment, when simply given the PCPs of each of 14 additional compounds, the ISTD provides reasonable approximations of the passive transport properties expected from *in vitro* experiments. Essentially identical passive transport estimates are also obtained for the same compounds when they are studied together in one ISTD experiment. The enzyme component is validated against a traditional two-site kinetic model along with *in vitro* metabolism data for benzyloxyresorufin: It exhibits substrate self-inhibition. Finally, the ISTD's suitability for exploring drug–drug interactions is demonstrated. Together the results represent an important, early advance in our ability to build pharmaceutically useful, scientifically informative models. To avoid confusion, including conflating the model with referent reality, and to clearly distinguish *in vitro* components and features, such as an enzyme, a drug, or metabolism, from corresponding in silico components and features, we generally use small caps when referring to the latter.

METHODS

We used the Swarm platform and libraries (http://www.swarm.org). It is the most mature of the agent-based modeling platforms (7). It facilitates building autonomous, articulable components (capability 8 in Appendix) that can be plugged together to form an analogue system following the synthetic modeling method. We coded in Java Swarm. Doing so gave direct access to Swarm's Objective-C libraries and enabled the created software to be easily integrated with statistical and mathematical software, such as R and Matlab, for post-simulation data processing. The code may be obtained from the authors. We conducted data analysis, parameter optimization, graphing, and mathematical modeling in Matlab version 13. We repeated all simulations 20–50 times; results are reported as arithmetical mean values, unless otherwise noted. We verified that the central limit theorem holds for all observations. From inspection of Q–Q plots or application of the Shapiro–Wilsk test, we concluded that normality assumptions are valid for all observations. When parameter optimization was required, we applied standard nonlinear fitting algorithms provided in Matlab until convergence was achieved.

Model Structures and Assumptions

The ISTD structure illustrated in Fig. 1 mimics the structure of a Transwell device (TD). Its framework and features are extensions of those detailed in (1), but are refined and augmented to enable delivering the nine capabilities listed in the Appendix. The ISTD represents an arbitrary-width, square column section through an entire TD. The section is subdivided vertically into five spatial components, designated S1–S5. Each is discretized further using a 2D square grid, the dimensions of which control the lower limit of spatial resolution and control the precision of the simulated behaviors. Each grid of 100×100 elements has toroidal boundaries. Together, the 10^4 elements comprising each space represent the content of a corresponding part of the TD or a portion thereof. For example, each element of S1 maps to 0.01% of the fluid in the apical TD compartment. Elements in S2 and S4 map to portions of the apical and basal cell membranes, respectively. The volumetric nature of each S1–S5 element is simulated by placing at each grid location a software object that acts as a container having an arbitrary but specifiable capacity (a virtual volume). The capacity of different elements can be analogous to pharmacokinetic compartments having different volumes of distribution. An element's capacity is adjustable; in this report, it is identical within each space, but different between spaces. These elements can have arbitrary shapes, but in this report, each is treated as an hexahedron with parallel sides as illustrated in Fig. 1. An element is identified and labeled with relevant chemical properties. For example, each element of S1 is assigned whatever aqueous properties are required for the experiments planned, such as pH (in silico pH), ionic strength, etc. For this report, the effective capacity of each element is given by a relative (with respect to cell membrane) "height" parameter (H) that maps to the height of that space in the referent TD. The values used are listed in Table I and are those reported in (8) and (9). Elements of S2 and S4 are treated as having a capacity of 1.0 U^3. Relative to an element of S2, an element in S1 shares an interface with S1 and has a capacity of 5.5×10^5 U^3. The resolution of S1–S5 can be easily increased when required.

Objects are also used to represent other fixed and mobile components. For this report, they are limited to mobile compounds (also called drugs), fixed enzymes, and fixed tight junction pores (or simply pores). As was done in (2) and (6), components can be added to S2 and S4 when needed to represent transporters or other cell membrane components.

Discrete Event Schedules

Discrete event simulation can be more efficient than discrete time simulation (10). ISTD simulations are advanced using dynamically scheduled discrete events. For discrete time simulations, the state of each component is updated at fixed intervals, regardless of whether or not an event takes place. For discrete event simulations, computations are executed only when the state of a component changes. The ISTD uses agents at two different levels to direct and manage event scheduling. At the bottom level, three agents, *ScheduleTransitEvent*, *ScheduleLateralEvent,* and *ScheduleEnzymeEvent*, manage the progress of compound relocation and transition into adjacent spaces, lateral diffusion within each space, and metabolism (discussed below), respectively. Above these agents is the master *ScheduleEvent* agent; it oversees and coordinates the activities of the other three. We used a hierarchical heap tree data structure (11) to facilitate dynamic scheduling. Doing so enabled efficient event insertion, deletion, and exchange to be accomplished on the order of log$n$ time: n is

Table I. ISTD Parameters

Category	Name	Description	Values
ISTD	*worldXSize*, *worldYSize*	Dimensions of S1–S5	100×100
	tightJunctions	Fraction of area covered by occupied by pores	0 to 0.001
	tjSize	Pore radius	0 to 16 Å
	numENZ	Number of enzymes in S3	40
	cellularpH	Simulated pH in S3	7.2 to 7.4
	S1 thickness	The relative thickness of S1	5.52×10^5
	S2 thickness	The relative thickness of S2	1^a
	S3 thickness	The relative thickness of S3	2.0×10^3
	S4 thickness	The relative thickness of S4	1
	S5 thickness	The relative thickness of S5	3.19×10^5
	memPotential	The transmembrane potential	−57 mv
Physicochemical properties of compounds	*molecularWeight*	MW	100 to 500
	isAcid	Drug: a weak acid (otherwise, weak base)	T or F
	p*K*a	Drug's p*K*a	4 to 14
	logP_{ow}	Logarithm of partition coefficient	−5 to +5
	ionDiffusion	Permeation due to ionized form of drug (%)	0 to 1
	substrateOfENZ	Drug is a substrate of the enzyme	T or F
	s1Prob	Probability of binding to s1	0 to 1
	s2Prob	Probability of binding to s2	0 to 1
	MProb	Probability that metabolite is formed	0 to 1
	α	Enhancing factor for the 2nd site binding	0 to 5
	β	Inhibition factor for metabolism	0 to 1
Experimental condition	*numSolutes*	Initial amount in S1 or S5	0 to 40,000
	drugTypes	Types of drugs in the simulation	1 to 14
	s1pH	Simulated S1 (apical) pH	5 to 8
	s5pH	Simulated S5 (basolateral) pH	7.4
	a2bDirection	Donor is S1 (or S5)	T or F

[a] Based on a membrane thickness of 7.5–10 nm.

the number of current events in the heap tree. The hierarchical structure was such that schedule changes occurring under one scheduling agent did not affect other schedules. Additional scheduling agents can be easily added as the system evolves.

Movement of Compounds

As in (1,2,5, and 6) a compound represents m ($m \geq 1$) drug molecules. One compound located in one element of S3 (for one simulation cycle) represents the average number of molecules occupying a corresponding volume of cytoplasm during a 5 s interval. In this report, m is always large. The relative in silico behaviors of different compounds within the ISTD are intended to map to those of different drugs *in vitro*; they are also expected to convey relative differences in PCPs. Prior to the start of an in silico experiment, a certain dose of compound is added to one space, typically S1. Within the five spaces, compounds are uniformly distributed among elements, representing a uniform concentration within the corresponding *in vitro* space. Each compound is identified and labeled with values that map to selected PCPs of a referent drug, such as pK_a, octanol–water partition coefficient P_{ow}, molecular weight (MW), etc. Any number of different compounds can be studied simultaneously and tracked individually in the same ISTD. However, no distinction is made between simulated molecules of the same type. This design feature enables capability 9 in the Appendix.

Simulation of Transcellular Passive Diffusion

In (1) simulation of passive diffusion relied on a globally specified concentration gradient. This gradient, rather than local, within-system events, controlled simulation outcomes. There are alternative, less deterministic ways to simulate passive diffusion. The pharmaceutical sciences literature is rich with examples of inductive, physical–chemical models being used to represent and predict different aspects of passive transport. Here, we explore the merits of adapting selected physical models to provide the logic for compound movement within and between ISTD elements. For simulated passive diffusion, we considered contributions from both transcellular and tight junction pathways. The logic adapted equations from (8,12 and 13). We estimated the cell membrane–aqueous phase partition coefficient for unionized compound (P_{cu}) at pH = 7.4 using $P_{cu} = d(P_{ow})^b$ (12), where P_{ow} is the referent compound's octanol–water partition coefficient. Using the alfentanil data reported in (13), we estimated $d = 0.437$ and $b = 1.328$. For simplicity, and because alfentanil is representative of the set of 14 compounds discussed under Results, we used those values for all simulations, although they could be made compound-specific. Following the lead of (13), we assumed that ionized compound could contribute to membrane–aqueous phase partitioning to a small degree: we arbitrarily specified the partition coefficient of the ionized compound to be $0.01P_{cu}$. We then computed an effective in silico membrane–aqueous phase partition coefficient as $P_c = P_{cu}(f_u + 0.01(1 - f_u))$; f_u is the unionized fraction of a simulated monoprotic weak acid or weak base in a given space. We limited attention to compounds having a single pK_a.

An unbound compound has two independent (separately scheduled) motions in a given space: lateral diffusion and (vertical) transition to a new location. Lateral diffusion is specified to be a random walk; consequently, the displacement to a new location within some interval Δt will follow a Gaussian distribution. We used a fixed update interval for lateral movement of $t = \Delta 5$ s. During that interval, each compound used one or more rules to decide whether or not to move to a new element. A rule served as a placeholder for in silico representations of more detailed mechanisms. We specified rules based on existing physical models that have been used successfully to describe similar processes. In each simulation cycle a position (x_t, y_t) within the same space was calculated by $x_t = x_0 + [\surd[4D_a\Delta t]\text{rv}\cdot\sin\theta]$ and $y_t = y_0 + [\ \surd[4D_a\Delta t]\text{rv}\cdot\cos\theta]$. ($x_0$, y_0) is the center of the compound's current grid location, rv is a random value drawn from a standard Gaussian distribution (mean = 0, SD = 1), θ is an angle drawn from the uniform distribution on $[0, 2\pi]$, and D_a is the referent compound's diffusion coefficient in aqueous solutions. D_a was calculated using the Stokes–Einstein equation (see Appendix) and was the same in S1, S3, and S5. Although the calculated, new position was precise, only the grid space of that new location was recorded. If the new grid location was occupied (e.g., by a pore or an enzyme), then the relocation calculation was repeated until successful.

As the simulation advanced, compounds in S1, S3, and S5 were repositioned "vertically": they were moved "up" (toward S1's air–media interface) or "down," as described below, relative to their current location in that virtual volume element. Compounds were also given an option to transit into an adjacent space. A compound that was "close" to a membrane interface, such as S3–S4, should have an option to transition (from S3 to S4) sooner than a compound that is "far" from that interface. To provide this option, beginning at the start of an experiment, every compound used a rule to schedule a transition opportunity at some future time, T_t; for compounds within S1, S3, and S5, that time was calculated using Einstein's 1D diffusion function: $T_t = T_c + (H - h_0)^2/.2D_a$. t_c is the current simulation time; H is the relative "height" of elements within the space in which the compound resides. h_0 is the compound's current location within that element. In S1, $h_0 = 0$ at the air–media interface, in S2 $h_0 = 0$ at the S1–S2 interface, and so on. At T_t, the compound calculated a new location for itself: $h_n = h_0 + Gaussian[0, (H - h_0)]$. Define $P_1 = P_c/(1 + P_c)$ and $P_2 = (P_c)^{-1}/[1 + (P_c)^{-1}]$; $(P_c)^{-1}$ as the effective in silico aqueous phase-membrane partition coefficient. For a compound in S1 or S5, when $h_n > H$ and a pseudorandom number (PRN) $\geq P_1$, it transitioned into the adjacent membrane space; otherwise, it was relocated randomly within its original element. When $h_n < 0$, it was randomly relocated within its original element. For a compound in S3, when $h_n > H$ and a PRN $\geq P_1$, it transitioned forward (away from the space in which the dose was placed) into that adjacent membrane. Otherwise, if a separate PRN $\geq P_2$, the compound transitioned backward into that adjacent membrane; if that PRN $< P_2$, it was relocated randomly within S3. All PRNs were drawn from a uniform [0, 1] distribution using a Mersenne Twister random number generator.

Upon arrival in S2 or S4, a compound again scheduled a transition opportunity at some future time: $T_t = T_c + (f + b)$

$H^2/2D_m$. H is the relative "height" of S2 and S4. $(f+b)$ is an estimate of the number of times in 10^{-5} s that a compound might transition from one side of the membrane to the other (forward, f; b, backwards; e.g., when dosed in S1, "forward" is from the S2–S1 interface to the S2–S3 interface). D_m is an estimate of the referent compound's membrane diffusion coefficient. Just like D_a, D_m was calculated using the Stokes–Einstein equation and from the *in vitro* alfentanil permeability data it was estimated to be $D_a/0.231 = D_m$ at 37°C (see Appendix). For simplicity, we used that same value for all other simulations. Define $P_3 = [1/(1+P_c)]^f [1/(1+(P_c)^{-1})]^b$; it is the probability that a compound fails to transition (e.g., to S1 or S3 if it is in S2) within 10^{-5} s. Define $P_4 = P_1/(P_1+P_2)$. If at T_t, a $\text{PRN} \leq P_3$, the compound stayed in the membrane. However, if that $\text{PRN} > P_3$ and a separate $\text{PRN} < P_4$, the compound transitioned forward (away from the originally dosed space) into the adjacent aqueous space. Otherwise, the compound transitioned backward to the aqueous space from which it came.

A compound was regarded as having been transported when it reached the acceptor compartment. To study simulated apical-to-basal permeability compounds were seeded randomly in S1. By enabling compounds to move both forward and backward, we were able to study permeability under non-sink conditions. Obtaining a measure of simulated effective permeability coefficient P_{eff} (the permeability coefficient of just the cell monolayer) was accomplished by conducting a control experiment in which the cell monolayer (S2, S3, and S4) had been removed: $(1/P_{eff}) = (1/P_{total}) - (1/P_{control})$.

Transit to and through Pores

Pores are container objects that represent the semiporous tight junctions between adjacent cells. Each one spanned S2, S3, and S4. They typically occupied no more than 0.1% of these three spaces. When a compound in S1 (or S5) was located "above" (or "below") a pore, for simplicity we defined a transition counterpart to P_c and specified it to be 1.0 for all compounds (it is treated as "partitioning" from one aqueous environment to another). As a result, P_1, defined above, became 0.5: the value can be tailored to each compound when that is needed. When $h_n > H$ and a $\text{PRN} \geq 0.5$, a compound "above" (or "below") a pore transited into the pore; otherwise, it was relocated randomly within the original element. The compound exited the pore either from its entry point or at the opposite end. To simulate passage through a pore we adapted rules based on the theoretical pore model described in (8) and (14). A compound in a pore scheduled an exit opportunity, as above, at some future time, $T_t . T_t = T_c + (H - h_0)^2/2D_p$. For a pore, H is the "distance" across S3, S2, and S4 and h_0 is the compound's current location within the pore. D_p is an in silico analogue of the paracellular, permeability coefficient in (8), calculated as described in the Appendix. At t_t, the compound calculated a new location for itself: $h_n = h_0 + Gaussian(0, [H - h_0])$. Conditional on a $\text{PRN} \geq 0.5$, if $h_n > H$, the compound exited into S5, but if $h_n < 0$, it exited back into S1; otherwise, it was relocated randomly within the pore.

Simulated Metabolism

One of the project goals has been to enable several different compounds to mingle together within the same simulated environment and have opportunities to interact with the same simulated enzymes and transporters. For clarity, all cytoplasmic components that can bind a referent drug, including drug-metabolizing enzymes, are conflated and represented collectively by identical objects: enzymes. One enzyme maps to e ($e \geq 1$) enzymes and may map to more than one type of metabolic enzyme. For this report, e is large and unspecified. Some metabolic enzymes, in particular CYP3A4, can exhibit non Michaelis–Menten characteristics in the presence of an inhibitor or an activator (in some cases it is the drug itself). CYP enzymes harbor at least two substrate-binding sites (15–18). For some substrates, reaction patterns have been observed consistent with self-activation and/or self-inhibition. To be scientifically useful, in silico CYP analogues need to be able to exhibit a full range of similar behaviors. We used a two-site enzyme such that simulated metabolic data validates against values calculated using specific parameterizations of the two-site kinetic model presented in (17): It has two binding domains within an active site and is described in the Appendix.

Upon initiating a simulation, a number of enzymes were randomly assigned to S3, one per element. Should different types of enzymes be needed, they can be represented by extending the class enzyme to sub-class objects that inherit the enzyme's logic. As diagrammed in Fig. 2, binding site s1 can generate a metabolite (M); the other, s2, cannot; however, binding to s2 can influence events at s1 and visa versa. An enzyme's state (and that of bound drug) is updated during each simulation cycle: 5 s was arbitrarily chosen as the cycle length. Enzymes are selected randomly for update at the start of each simulation cycle. Sites s1 and s2 are arbitrarily assigned to face in opposite directions, as indicated in Fig. 2. Consequently, as illustrated at the bottom of Fig. 3, they "see" different portions of the enzyme's local neighborhood. During a simulation cycle, drug in some locations within the local neighborhood was available to one site but not the other. The orientation of the enzyme could be specified prior to simulation or the enzyme could use local information to orient itself. For the results discussed here, orientations were random. We specified that any drug located "near" an enzyme—in the local neighborhood in Fig. 3—would have an opportunity to access that enzyme within a simulation cycle. For the current 5-s, simulation cycle, drug in any of the six locations within one of the two shaded areas had access to only one site during that cycle. Drug in the two unshaded locations ([2, 0′] and [2, 2′]) could access either site.

At the start of a simulation cycle, an enzyme exists in one of the four states depicted in Fig. 2. During a simulation cycle, a number of enzyme state changes can occur: each one is governed by a probability parameter. For example, the parameter *MProb* specifies the probability that a drug bound to s1 will be converted to a metabolite during that cycle. Seven probabilistic parameters are identified in both Figs. 2 and 3. The logic used by an enzyme during a simulation cycle is diagrammed in Fig. 3. It first surveys the local neighborhood and identifies the location of each drug, noting whether

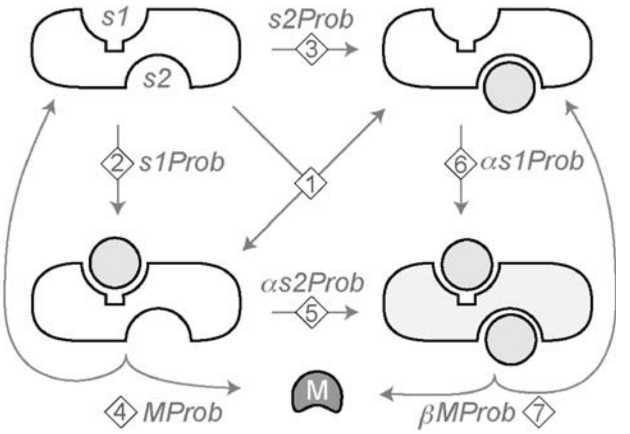

Fig. 2. The generic two-site, four-state, metabolic enzyme component. In this report we use it to represent CYPs. Each enzyme has two drug (substrate) binding sites, s1 and s2, that use the logic in Fig. 3 to interact (or not) with each compound in its local neighborhood. Those interactions can lead to state changes. A drug that binds to s1 (but not s2) may get converted to a metabolite (*M*). The numbers within diamonds (also indicated in Fig. 3) identify the enzyme's logic: seven questions (and their answers) that govern whether state change will occur within a 5-s simulation cycle and/or whether the drug will be converted to a metabolite. An answer to each question is provided by the value of at least one of the following five parameters. s1Prob is the probability that the considered drug will bind to s1 when s2 is free. s2Prob is the probability that the drug will bind to s2 when s1 is free. MProb is the probability the metabolite will form when s1 is occupied and s2 is free. α is the degree of inhibition (or enhancement) of s1Prob and s2Prob caused by a substrate occupying the other site. β is the degree of inhibition (or enhancement) of MProb caused by the substrate occupation of s2.

it is near s1, s2, or both. It then assigns each drug a randomly drawn number (a PRN drawn from [0, 1]). That value enables the enzyme to make decisions as it works through the logic in Fig. 3; those decisions determine the drug's fate.

Having drug bound to s1 during a simulation cycle can result in metabolism: It is governed by the parameter s1Prob (or αs1Prob when s2 is occupied). Having drug bound to s2 can influence metabolism but cannot cause it (however, it is easy to enable metabolism from s2 when that is needed). Binding to s2 is governed by the parameter s2Prob (or αs2Prob when s1 is occupied). Consider the case when both sites are vacant and a drug is near s1 and s2. If the assigned $PRN < s1Prob/(s1Prob + s2Prob)$, then the drug binds to s1 (the drug–s1 complex is formed). Otherwise, drug–s2 is formed. When drug–s1 is formed and the assigned PRN < Mprob, a metabolic product (M) is formed and released into an adjacent element (the drug object is deleted). However, if the assigned PRN ≥ MProb, the complex remains intact. For simplicity during these studies, only one M is formed each cycle.

Consider another case: at the start of the cycle, drug is bound to s1: the enzyme selects the drug near s2 that has the smallest assigned PRN. If that PRN < αs2Prob, it becomes bound to s2 resulting in a two-drug complex: the second bound drug influences metabolism. If a PRN < βMProb, a metabolite is formed and released into an adjacent element. Additional sequences of events are specified in Fig. 3. Alternative, equally valid methods are possible to manage the state changes in Fig. 2 during a simulation cycle, but we have not explored them. Following validation of the rules in Fig. 3, the relative probabilistic parameter values can be automatically adjusted to accommodate shorter or longer simulation cycles without altering the measured time-course of events.

RESULTS

Two categories of experiments were conducted: verification and validation. The extensive verification experiments provided evidence that an ISTD, as a software device, could be trusted to perform as intended: the transport properties under different conditions for a wide range of simulated compounds were consistent with wet-lab observations. The validation experiments showed that an ISTD can be tuned to provide permeability data that match those of specific compounds. Further, when given the properties of a specific compound, results from ISTD experiments can be made

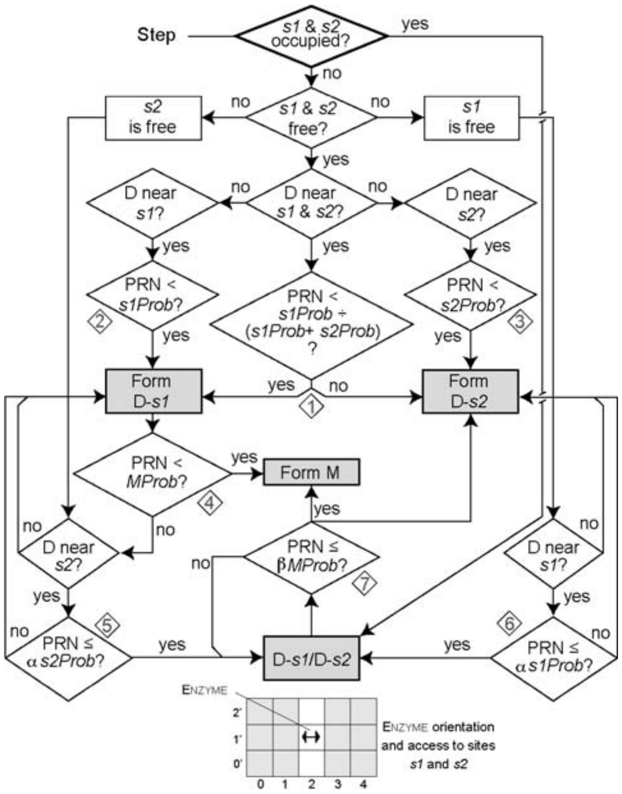

Fig. 3. A diagram of the logic followed by each metabolic enzyme during each simulation cycle. *D* Drug, *M* metabolite, *D–s1 (or D-s2)* drug bound to s1 (or s2), *PRN* a uniform pseudorandom number drawn from [0, 1]. The *numbers within diamonds* identify seven questions (also indicated in Fig. 2). The answer to each question determines which, if any, state change will occur and whether the drug is converted to a metabolite. The 5×3 grid below the diagram exemplifies an enzyme's local neighborhood. The enzyme is located at the central grid point (2, 1′). The *double arrow* indicates that s1 and s2 face in opposite directions. Assume that by chance s1 faces left. Drug in any one of the six gray grid spaces on the left have access to s1 (but not s2) during a simulation cycle. Drug in any one of the six gray grid spaces on the right have access to s2 (but not s1) during a simulation cycle. Drug at grid points (2, 0′) and/or (2, 2′) have access to both s1 and s2. Other local neighborhood management options were possible, but were not selected.

similar to those from wet-lab experiments. Stated differently, the validation results demonstrate that the Turing test capability stated in the Appendix has been demonstrated. Results from several types of verification experiments are described and presented in detail in Supplementary Material (SM) and we briefly summarized below.

Simulated Passive Transport

To verify that the analogue system can simulate passive transport consistent with *in vitro* observations, we conducted in silico experiments using compounds having the following range of properties; MW: 100 to 500; $\log P_{\mathrm{ow}}$: −5 to +5; $\mathrm{p}K_{\mathrm{a}}$: 4 to 14. In most simulation experiments, we assigned 0.066% of the represented area to pores (the reasons are discussed below). We then tuned pore size so that simulated urea transport was validated against the data reported in (8; also discussed below). The finalized pore radius mapped to 6.66 Å *in vitro*. Except where noted, we used those values.

We first measured the percentages of 55 different, unionized compounds remaining in S1 after 15 min; this duration was sufficient for random, "backward," compound movement to influence results. From the results (SM, Fig. S1), we calculated P_{total}; the data exhibited patterns similar to those reported in (12,19). The extent of transcellular transport was dominated by $\log P_{\mathrm{ow}}$. Very limited transport was observed for the most hydrophilic compounds, consistent with expectations. There was a modest decline in percent transported for the most lipophilic compounds (beginning at $\log P_{\mathrm{ow}}=3$). With increasing MW, the percent of dose transported also decreased. These behaviors were emergent properties of the local mechanisms: they were not prespecified. Results when dosing to S5, rather than S1 (not shown), were similar.

Additional experiments verified the combined influence of $\mathrm{p}K_{\mathrm{a}}$ and $\log P_{\mathrm{ow}}$. Both exerted a considerable influence on simulated transport. Each of 84 different, small (each having MW = 100), weak base, compounds was studied (SM, Fig. S2). The data show that the influence of $\mathrm{p}K_{\mathrm{a}}$ is most dramatic for compounds having $-1 \le \log P_{OW} \le 1$: the influence of $\mathrm{p}K_{\mathrm{a}}$ decreased as $\log P_{\mathrm{ow}}$ deviated from zero. For the six most hydrophilic compounds ($\log P_{\mathrm{ow}}=-2$) that were mostly ionized ($\mathrm{p}K_{\mathrm{a}}\ge 9$), essentially all of the simulated transport was via pores. The relative contribution of pore transport decreased with decreasing $\log P_{\mathrm{ow}}$ and $\mathrm{p}K_{\mathrm{a}}$ values.

Simulated Transport Through Tight Junctions

The normal, effective pore radius for confluent Caco-2 monolayers was reported in (8) to be about 4.6 Å. When perturbed, the effective radius increased to an average of about 14.6 Å. With that range in mind, we simulated pores having radii ranging from 0 to 16 Å. We simulated transport for each of eight weak base compounds ($\mathrm{p}K_{\mathrm{a}}$: 4–10) having MW = 100. To maximize the relative amount that transited through pores, we specified $\log P_{\mathrm{ow}}=-2$ for each. The percent of total transport to S5 (starting from S1) that was a consequence of transport through pores was calculated (SM, Fig. S3). When the ionized fraction is significant, increasing pore radius significantly increased transport through pores, and the effect of $\mathrm{p}K_{\mathrm{a}}$ was dramatic. Increasing pore radius further had an insignificant effect.

We also examined the effect of pore size on simulated transport for sixty hydrophilic ($\log P_{\mathrm{ow}}=-2$), neutral compounds having MWs in the range 100 to 500. The effect of increasing pore size was nonlinear. Even after 50 min, when the pore radius was 16 Å, only about 2.2% of the MW = 500 compound reached S5 (SM, Fig. S4a). For the pore radii range of 4.5–7 Å, which is typical for confluent epithelial cell monolayers, less than about 1% of the compounds having MW ≥ 200 reached S5 within 50 min. As expected, MW had a dramatic influence on the fraction reaching S5 (SM, Fig. S4b).

Reports of the percentage of cell culture areas assignable to porous tight junctions range from 0.01 to about 0.1% (20,21). Observing the consequences of changing pore density provides useful verification information: halving density should halve the percent transported through tight junctions, while decreasing density should linearly increase the percent of transcellular transport. The results of such experiments showed a reasonably linear relationship between pore density and percent transported, and between pore density and mean percent transcellular transport for all four pore sizes (SM, Fig. S5).

Validation and Prediction: Passive Transport

The validation of a model is defined (22) as "the process of determining the degree to which a model or simulation is an accurate representation of the real world from the perspective of the intended uses of the model or simulation." Face validation is "the process of determining whether a model or simulation seems reasonable to domain experts, based on the model's performance." Structural validation is the process of determining that the assumptions, algorithms, and architecture provide an accurate representation of the composition of the real world as relevant to the intended use." The above verification experiments also provided essential face and structural validation evidence.

We began validation with urea (MW = 60; $\log P_{\mathrm{ow}}=-2$). Although mannitol is preferred for measuring pore permeability *in vitro*, we elected to validate against urea data in part because there is a small amount of transcellular transport. Urea permeates slowly through confluent Caco-2 monolayers (8), primarily through semi-porous tight junctions. We iteratively tuned pore surface density and radius and compared simulated with *in vitro* data up to 3 h. The results in Fig. 4 were judged by inspection to be acceptable: the pore density was 0.066% and pore radius mapped to 6.66 Å *in vitro*. Both values are within reported ranges (12,23). Results of transport through pores and through cells for a typical single experiment are shown, along with the 95% confidence intervals of measurements ($n=30$) made every 60 s. Within the data from the single experiment, a decline in the accumulated urea is a consequence of the realistic net random movement of some urea objects from S5 back toward S1. More than 96.3% of the transported urea arrived in S5 through pores.

We also estimated the total permeability of mannitol (MW = 182; $\log P_{\mathrm{ow}}=-3.506$, neutral), based on the data that showed around 0.1% of mannitol should reach S5 by 15th minute (see SM, Fig. S1). A mean P_{total} of 2.06×10^{-7} cm/s

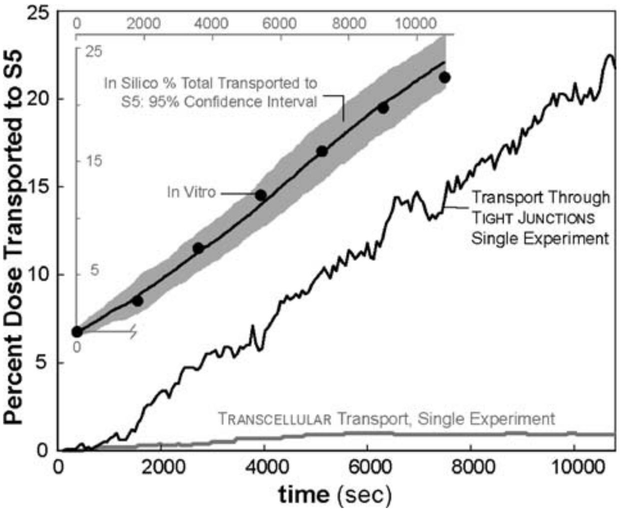

Fig. 4. Validation of passive transport within the ISTD using *in vitro* urea transport data. A dose of 1,000 compounds representing urea (MW = 60 and log$P_{\mathrm{ow}} = -2$) was added initially to S1; simulations were repeated 30 times. The number of urea transported to S5 was recorded every 60 s until the third hour. Pore density and pore radius were iteratively auto-adjusted until the transport data matched the 3-h, *in vitro*, urea transport data reported in (8). A pore density of 0.066% and pore radius of 6.66 Å gave the results shown. The central jagged line shows the number of urea that had accumulated in S5 at the indicated times during one typical simulation. The *lower gray line* shows the number of urea transported transcellularly to S5 during that same experiment. The *insert* shows the mean values of trans-pore, paracellular transport for 20 simulations along with the in silico 95% confidence interval (*gray area*). The *black circles* are the *in vitro* data from (8).

was obtained. That falls between the mean P_{total} of 2.37×10^{-7} cm/s in (8) and 1.51×10^{-7} cm in (13).

We fixed the two pore parameters to the values stated above and then began validation against alfentanil data. Alfentanil is a lipophilic, weak base: MW = 416, log$P_{\mathrm{ow}} = 2.16$ and p$K_{\mathrm{a}} = 6.5$. It rapidly permeates Caco-2 monolayers. It is known not to be a significant substrate of efflux transporters. The fact that metabolism is negligible *in vitro* makes alfentanil an ideal compound for validation of passive, transcellular transport and is representative of the set of 14 other compounds studied below. *In vitro* permeation data are available over a range of donor compartment pH conditions (13), and it is against these data that we validated.

Any intracellular non-specific binding has been conflated into the probability of exiting S3, but can be factored out as needed. The pH of S1 was varied from 5.0 to 8.0 to match *in vitro* experiments. The pH in S3 and S5 was held constant at 7.4. In silico values of P_{eff} were calculated as described in "Methods." The results in Fig. 5a agree closely with the *in vitro* P_{eff} values, which were measured experimentally for different donor compartment pH values and then fit by a carefully reasoned mathematical model (see Appendix). The similarities between *in vitro* and in silico values are as close, if not closer, than between the *in vitro* and mathematical model values reported in (13). We compared the time-series transport values from that parameterized, mathematical model with the ISTD-generated values in Fig. 5b by calculating their ratios. The results are graphed in Fig. 5b for the control and three pH values: 5.0, 6.5 and 8.0. The ratios for pH 6.5 are representative of the ratio values for the other six pH conditions that are not plotted. All ratios approached 1.0 with increasing time; the largest difference in predictions occurs prior to 300 s, when assumptions of ideality underlying the mathematical model do not map to events occurring within the ISTD. More specifically, the mathematical model assumes bulk flow and ignores the volume of cells. Consequently, there was no lag-time. The ISTD did not use those assumptions. The simulations showed a short lag time before compounds began reaching S5. Therefore, initially ($t \leq 30$ s), the ratios of the two models are bigger than 1.0. During this interval, compounds accumulated in S3, which

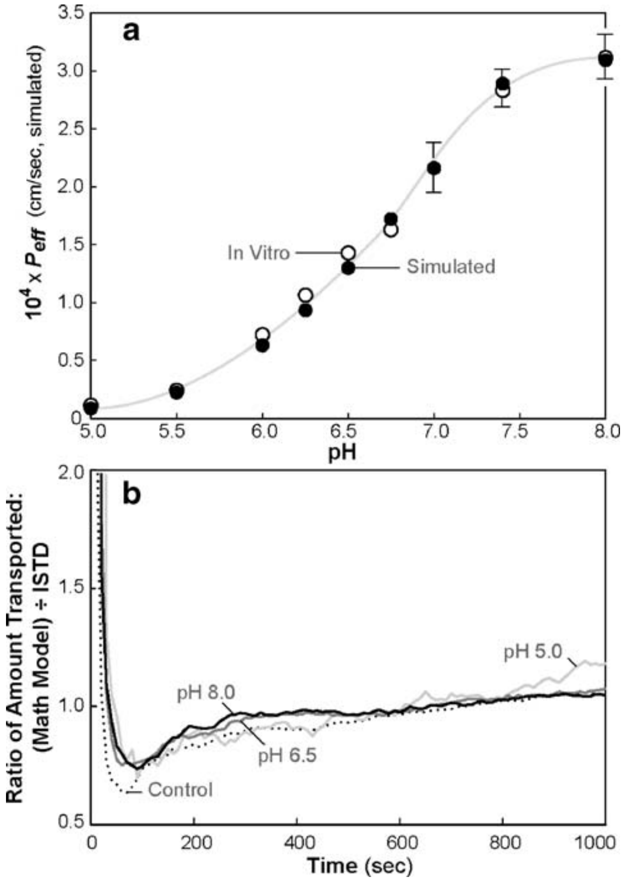

Fig. 5. Validation of passive transport within the ISTD using *in vitro* alfentanil transport data. All ISTD-specific parameter values were the same as those used to match the urea in Fig. 4. Only D_{a} for alfentanil was tuned to obtain the match shown. A dose of 1,000 alfentanils was added initially to S1; simulations were repeated 20 times. The number of alfentanil transported to S5 was recorded for 1,000 s. **a** Mean P_{eff} values for alfentanil from *in vitro* experiments (*open circles*) and for alfentanil (*filled circles*) are plotted *vs* pH of the apical (S1) compartment. *Vertical bars* Standard deviations (for most experiments they are covered by the *filled* and *open circle*). The *gray curve* is a trend line. **b** Transport from two models are compared. The amount of alfentanil transported to the basal compartment *in vitro* for each of nine apical compartment pH values was calculated using the mathematical model in (8) that had been fit to the data in **a**. The corresponding simulated values were determined from the in silico experiments in **a**. The ratios of these values are plotted *vs* time for three selected pH values (5.0, 6.5, and 8.0) and the control. The ratio values for the other six pH conditions were similar to the pH 6.5 values.

Table II. Physicochemical Parameters of 14 Drugs

Name[a]	MW	pK_a	Acid/Base	logP_{ow}	Linear Model logP_{eff}	*In Vitro* logP_{eff}	ISTD logP_{eff}	ISTD logP_{total}
Amiloride	230	5.26	Base	−0.20[b]	−4.26	−3.79	−4.08	−4.25
Antipyrine	188	1.4[c]	Base	1.79	−3.24	−3.35	−3.63	−3.99
Atenolol	266	10.1	Base	0.44	−4.53	−4.7	−4.82	−4.86
Cimetidine	241	6.71	Base	−0.09	−4.36	−4.52	−4.05	−4.23
Desipramine	266	10.6	Base	4.00	−3.50	−3.36	−3.68	−4.03
Fluvastatine	411	4.32	Acid	4.71	−3.44	−3.62	−3.70	−4.08
Furosemide	331	4.06	Acid	−1.06[d]	−4.58	−5.3	−5.34	−5.35
Ketoprofen	254	3.49	Acid	3.67	−2.81	−3.08	−3.68	−4.02
Metoprolol	267	10.1	Base	1.97	−3.82	−3.89	−3.76	−4.07
Naproxen	230	4.06	Acid	3.26	−3.14	−3.08	−3.64	−4.01
Piroxicam	331	4.66	Base	0.45	−4.17	−3.11	−3.80	−4.1
Propranolol	259	10.1	Base	3.00	−3.73	−3.54	−3.65	−4.02
Ranitidine	314	9.04	Base	0.79	−4.55	−4.57	−4.21	−4.35
Terbutaline	225	12.0	Base	1.07	−4.31	−4.52	−4.27	−4.38

[a] Drugs, their PCPs, and *in Vitro* logP_{eff} are taken from Table I of (14). Except for antipyrine, drugs with one or more missing values were not selected.

[b] The value was set to −0.20 according to (26); the value was −1.03 in (14).

[c] The value was set to 1.4 according to (27).

[d] The value was set to −1.06 according to (28); the value 2.0 in (14) led to under-estimates, which were discussed by Obata *et al. (14).*

caused a subsequent surge in compounds reaching S5. But, there were no such events in the mathematical model. As a result, sub-sequentially ($30 \leq t \leq 300$ s) the ratios of the two models become smaller than 1.0.

Having adjusted the in silico D_a for alfentanil so that the ISTD validated against referent data, we assessed how well that ISTD would predict logP_{eff} values for other compounds when given only MW, logP_{ow}, and pK_a, without any further ISTD refinement. We focused on 14 of the passively transported compounds reported in (14). The PCPs are listed in Table II. The resulting ISTD-predicted logP_{eff} values are graphed in Fig. 6. The correlation coefficient was 0.885 and the residual sum of squares was 1.88. For comparison, we fitted the same *in vitro* data using a classical, linear, multivariate model that used the PCPs in Table II. The result was $\log P_{eff} = -2.80 - 0.004MW - 0.06pK_a + 0.30\,logP_{OW} - 0.129c$; c is a binary variable: for a weak base, $c = 1$; for a weak acid, $c = -1$. The correlation coefficient for this model was 0.823 and the residual sum of squares was 2.13.

The Two-Site Analogue of Metabolizing Enzymes

An advantage of the synthetic modeling method is that components can be verified and validated separately. The resulting, validated component will reliably retain that verified functionality when plugged into composite components such as S3. The enzyme in Fig. 3 was intended to mimic the two-site kinetic model for substrate inhibition in Scheme 5 and equation 11 in (17). Our expectation was that data obtained from operation of these enzyme objects could be fitted by the referent kinetic model. To verify that, we conducted five cross-model validation experiments. Enzymes were parameterized as specified in Table III. In all five cases, s1Prob and MProb were held constant at 0.5 and 0.05, respectively. Except for s2Prob = 0 in the control case, which results in an enzyme exhibiting simple Michaelis–Menten kinetics, s2Prob was held constant at 0.05 in the other four cases. Also, in those four cases, the α/β ratio for the enzyme ranged from 2 to 50. Only the S3 space was used, simulating an *in vitro* metabolism study using microsomes isolated from rat hepatocytes; pore density was set to zero. The test compound had these properties: MW = 301.5, logP_{ow} = 2.11, and pK_a = 7.4. Forty enzymes were placed randomly in S3. Initial substrate levels ranged from 100 to 40,000. All simulations were terminated after 35 s, which was adequate to calculate initial reaction rates. Because only a few compounds bind or get metabolized in 35 s, 50 experiments

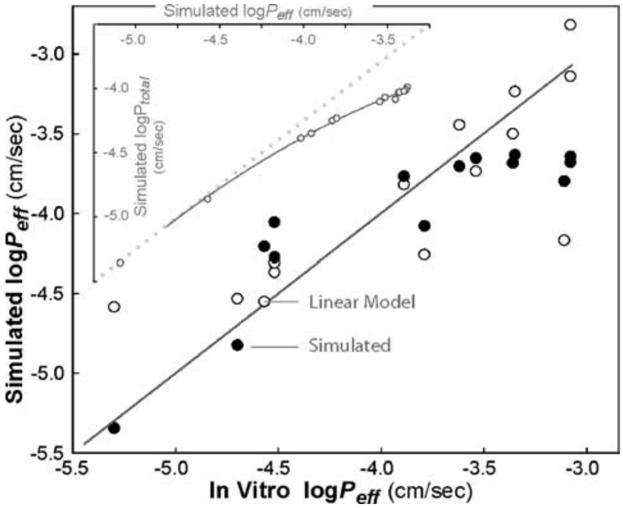

Fig. 6. Predicted logP_{eff} values from two models are compared. First model: the ISTD was parameterized and 30 experiments were conducted as in Fig. 5 for each of the 14 drugs in Table II. *Closed symbols* Mean logP_{eff} value for each compound is plotted against its *in vitro* counterpart. The correlation coefficient is 0.885. Second model: the 14 *in vitro* logP_{eff} values were fit to the four-variable, linear model described in the text. *Open symbols*: the logP_{eff} value for each drug, calculated from the fitted, four-variable linear model, is plotted against its *in vitro* counterpart. The correlation coefficient is 0.823. The straight gray line: $y = x$. *Insert* logP_{total} values from the simulated experiments are plotted against the corresponding logP_{eff} values, for each of the 14 drugs. The deviation logP_{total} = logP_{eff} is due in part to absence of stirring in the current ISTD.

Table III. Comparison of Parameters Between ISTD and Classical Kinetic Model

ISTD[a]	Kinetic Model[b]								
α	s1Prob	s2Prob	β	MProb	α'	KS (μm)	KI (μm)	β'	*V*max nmol/min
0	0.5	0	0	0.5	0	3.64	0	0	221.93
5	0.5	0.05	0.5	0.5	0.36	4.51	51.19	0.61	224.36
1	0.5	0.05	0.5	0.5	0.54	5.25	63.09	0.51	258.01
5	0.5	0.05	0.1	0.5	0.26	4.98	38.10	0.37	236.43
1	0.5	0.05	0.1	0.5	0.47	6.32	50.55	0.30	287.85

[a] ISTD parameter values used to obtain the data in Fig. 7.
[b] Described in Appendix; parameter values obtained from the best fit of the data in Fig. 7.

were conducted for each set of enzyme properties. The initial reaction rates were plotted (Fig. 7). The referent kinetic model was then fitted to the simulated data using least squares regression, assuming the content of S3 maps to a 1 μM solution; that amount of solute was represented by 600 compounds. Values calculated from the five fitted equations are graphed in Fig. 7; the fitted parameter values are listed in Table III. For the control case (s2Prob = 0), there should have been no evidence of inhibition, and there was none. For the other cases, when α was fixed and α/β increased, the maximum reaction rate decreased but the degree of inhibition increased; when β was fixed and α/β increased, both the maximum reaction rate and the degree of self-inhibition decreased. In addition, when α/β was fixed, the same maximum reaction rate was maintained, but larger α or β values lead to less self-inhibition. Note that although MProb, s1Prob, and s2Prob were held constant at 0.5, 0.5, and 0.05, respectively, each set of K_S, K_i and V_{max} values in Table III for the fitted kinetic model are unique. This observation illustrates that the mapping between parameter values in the two model types is neither simple nor straightforward: they are two different models that can generate the same observables.

The metabolism of benzyloxyresorufin to resorufin by P450 3A4 exhibits self-inhibition. Shou *et al.* (17) fitted data for that transformation to the two-site kinetic model described above. We replicated that fit. The results are graphed in Fig. 8a. We then used S3 from Fig. 7 with zero pore density and 40 enzymes and set compound PCPs to correspond to benzyloxyresorufin (MW = 303.3; P_{ow} = 3.64). Experiments were conducted as in Fig. 7. To map our simulation results to the data in (17), we specified that 600 benzyloxyresorufins in the S3 space represented 1 μM benzyloxyresorufin. We iteratively tuned the five enzyme parameters. Initial reaction rates were obtained from data collected during the initial 35 s of simulation. Each experiment for the final parameterization was repeated 30 times and the results averaged. Results from a match, judged acceptable by inspection, are shown in Fig. 8b. The error bars show the standard error of the mean for the simulated data.

Multiple Compounds, Same Simulation Experiment

Achieving capability 6 is an important objective: the ISTD must be reusable for simulating the absorption and transport of multiple compounds in the same simulation, not just one compound in each separate simulation. All of the preceding simulations were conducted using just one compound type. The objects and agents within the ISTD are capable of distinguishing between any numbers of different compounds. To verify that capability, we repeated the experiment in Fig. 6, but added all 14 compounds to S1 at the same time. Little interaction was expected because the transport of each compound was passive. However, there could be competition for pore access. The simulations were repeated 30 times. The results are graphed in Fig. 9. The difference between the two sets of results (Figs. 6 and 9) was within the range for ISTD experimental variability. The ratio

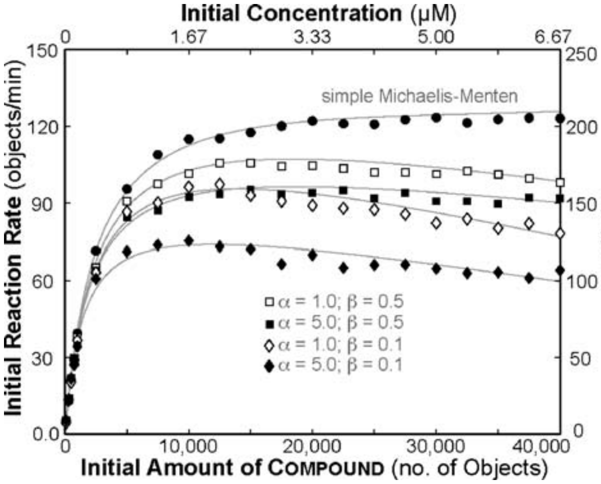

Fig. 7. Verification of the two-site enzyme component. Prior to initiating simulation, 40 enzymes were randomly placed in S3. Five different drug types were studied; however, they share the same PCPs (MW = 301.5, logP_{ow} = 2.11 and pK_a = 7.4). For each simulation, a dose of 100 to 40,000 drug objects of the same type was added to S3. Pore density was set to zero. The production of released (from an enzyme) metabolites was measured for 35 s; initial reaction rates were calculated for 50 experiments per condition. The *left* and *bottom axes* are the actual in silico values; the *right* and *upper axes* allow the simulated data and their fitted kinetic parameter values to be compared to the data in Fig. 8. Simple Michaelis–Menten (*top curve*): s2Prob between enzymes and drug was set to zero to verify that the resulting ISTD would exhibit simple Michaelis–Menten kinetics. The other four drug types had s1Prob = MProb = 0.5 and s2Prob = 0.05 along with the listed α and β values in Table III. The *right* and *upper axes* assume that 600 compounds in the S3 space mapped to 1 μM substrate. The simulated data were fit to the two-site kinetic model from (17; the equation is provided in the Appendix); the *curves* are the best fits (least squares). The fitted parameter values are listed in Table III.

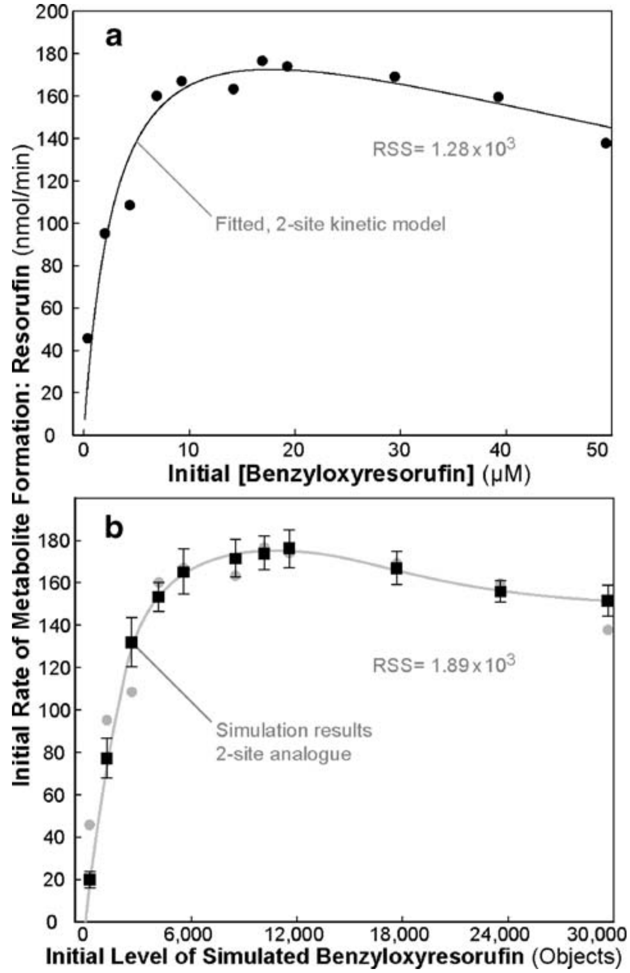

Fig. 8. Validation of enzyme functionality within the ISTD. **a** The target data, *in vitro* metabolite formation rate (*filled circles*) for different initial concentrations of benzyloxyresorufin, were taken from (17) and fit to the two-site kinetic model as discussed in the text (see Table II). The curve shows the predicted values. The residual sum of squares (RSS) is shown. **b** Simulated metabolite formation rate measures for different doses of objects representing benzyloxyresorufin: 600 objects in the S3 space mapped to 1 μM benzyloxyresorufin. The experiments were conducted as in Fig. 7. The *black squares* are mean values (±standard error of the mean, $n = 30$). The *gray circles* are the values from **a** replotted for comparison. The *gray curve* is the trend line. The residual sum of squares (*RSS*) is shown.

of correlation coefficients from Figs. 6 and 9 data was 0.885/0.881 = 1.005. The insert in Fig. 9 is a plot of the values for $\log P_{\text{total}}$ and $\log P_{\text{eff}}$ determined separately for each of the 14 compounds *vs* the corresponding values determined when all 14 were simulated in the same experiment. For $\log P_{\text{total}}$ values, the correlation coefficient was 0.998; for $\log P_{\text{eff}}$ values, it was 0.992.

Finally, we conducted simulations to verify that the ISTD with 40 enzymes added randomly to S3 can be used to simulate drug–drug interactions. We used two compounds (any number of different types can be studied), both having the same PCPs: MW = 301.5, $\log P_{\text{ow}} = 2.11$, and $\text{p}K_{\text{a}} = 7.4$, as in Fig. 7. For simplicity, we inactivated the s2 site by setting s2Prob = 0 to obtain simple Michaelis–Menten kinetics. The target compound had s1Prob = 0.5 and MProb = 0.5; initial S3 compound levels ranged from 100 to 40,000. Initial reaction rates were calculated as in Fig. 8 using data from the first 35 s of simulation. Experiments were repeated 50 times; mean values were plotted. In the first set of experiments, 10,000 inhibitors (MProb = 0.5 with s1Prob = 0, 0.25, or 0.5) were added initially along with the target compound. One inhibitor, like one compound, maps to a large number of inhibitors molecules *in vitro*. The results are graphed in Fig. 10a. The linear Lineweaver–Burke plots (the insert) intersecting at the same 1/(initial velocity) value are characteristic of classical single-site competitive inhibition. We similarly studied the consequences of having different initial quantities of inhibitor in S3: none, 5,000, 10,000, and 15,000. The parameter values for the inhibitor were MProb = 0.5, and s1Prob = 0.5. The results are plotted in Fig. 10b. The sigmoid curves are characteristic of classical, competitive inhibition.

DISCUSSION

In Silico to *In Vitro* Mappings

In vitro models have proven to be useful research analogues for research into selected aspects of organisms. When useful, there is a mapping between the two systems' observed phenomena. Stated differently, an *in vitro* model will be most useful when its phenotype overlaps phenotypic attributes of the *in vivo* system. Within the region of overlap, a mapping may also exist between the mechanisms underlying the measured phenomena. As many *in vitro–in vivo* correlation studies have demonstrated, the mappings may be neither simple nor linear. Often components are different on several levels. An *in vitro* model is an abstract representation designed for specific uses with specific expectations. One-to-one congruence at all levels is infeasible. The relationships

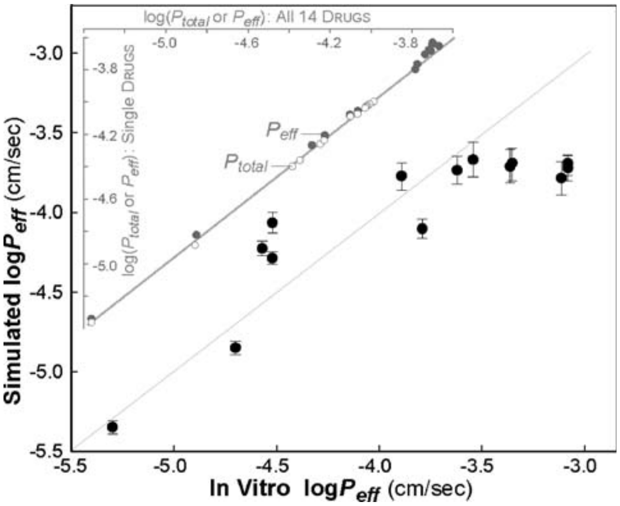

Fig. 9. Predictions of $\log P_{\text{eff}}$ values from co-administration of multiple drugs. All 14 compounds (1,000 each) in Fig. 11 were added to S1 with the ISTD parameterized as in Fig. 6. Thirty experiments were conducted as before: $\log P_{\text{total}}$ and $\log P_{\text{eff}}$ values were calculated. Mean simulated values (±standard error of the mean) are plotted against corresponding *in vitro* values: correlation coefficient = 0.881. The *straight gray line* $y = x$. *Insert* Mean $\log P_{\text{total}}$ and $\log P_{\text{eff}}$ values from the individual experiments in Fig. 6 are plotted against the corresponding mean values from this experiment. Correlation coefficients are 0.998 and 0.992, respectively.

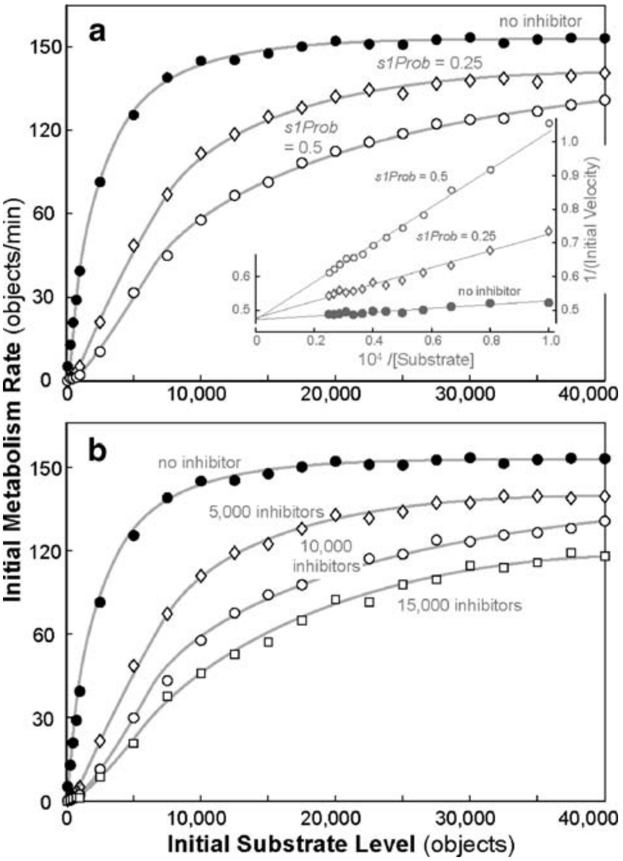

Fig. 10. Simulated drug–drug interactions. ISTD experiments were conducted as in Fig. 7; S3 contained 40 enzymes and the drug too had the same PCPs as in Fig. 7. However, except for the control experiments, an inhibitor having the same PCPs as the drug was also added to S3. For the drug, s1Prob = MProb = 0.5 and s2Prob = 0. **a** *Black circles* Initial metabolism rate is plotted against initial S3 substrate (drug) level in the absence of inhibitor (control). *Open symbols* Initial metabolism rates when 10,000 inhibitors were added to S3 along with drug. In one case, s1Prob = 0.25 and MProb = 0.5 for the enzyme–inhibitor; in the other case s1Prob = MProb = 0.5. The *gray curves* are trend lines. *Insert* A Lineweaver–Burke plot of the same data. **b** *Black circles* Initial metabolism rates for the control experiments are replotted. *Open symbols* Initial metabolism rates when the three indicated amounts of inhibitors were added to S3 along with drug; for enzyme–inhibitor interaction, s1Prob = M-Prob = 0.5. The *gray curves* are trend lines.

between an in silico model such as the ISTD and its *in vitro* counterpart are expected to be similar to those between *in vitro* models and their *in vivo* counterpart. By studying the *in vitro* system, we intend to gain deeper insight into how the *in vitro* system may be working. By analogy, we want in silico models capable of facilitating deeper insight into how *in vitro* systems actually work: we desire overlap, but not identity, between in silico and *in vitro* system phenotypes and mechanisms. With that overlap, there can be useful, predictive mappings between the two system phenotypes and their mechanisms. An advantage of this class of in silico models is that once one model has been validated against an *in vitro* counterpart, it can be modified and extended (morphed) to simulate aspects of the *in vivo* referent of the *in vitro* system.

An *in vitro*-to-*in vivo* mapping could, for example, compare relative features of *in vitro* treatments to corresponding observations *in vivo*. Specifically, when *A* is metabolized more extensively than *B* by CYP 3A4 *in vitro*, the same ranking is expected *in vivo*. To make the prediction quantitative, a transformation is needed; the transform itself is a model. It is impracticable to merge a model that enables quantitative *in vitro*-to-*in vivo* transformation with an *in vitro* wet-lab model: they are kept separate, and predictive, transformation models are often developed and applied after the fact. Should features enabling direct comparison of vitro observables, such as rate of change of drug concentration in the receiver compartment, with ISTD observables be built into the ISTD or should they be kept separate, as in the *in vitro*-to-*in vitro* case? The validation process started here will help answer that question. For these studies, we elected to make simulated time directly represent *in vitro* time and to make the simulated elements directly comparable to their *in vitro* counterparts with the expectation that results from the validation experiments in Figs. 4 and 5 would become simple and intuitive. However, the interpretation of other features such as compound objects in S3 is left unspecified until a comparison is made with specific *in vitro* data, as in Fig. 7.

Discretization and Resolution

An advantage of using discrete event models in this context is that they allow the researcher to control the limits of resolution (system granularity) and manage some of the uncertainty. Below these levels of resolution, there is uncertainty (it may range from limited to complete). Nevertheless, systemic events and behaviors can be simulated by using software logic (typically rules, axioms or principles) as placeholders for *in vitro* details about which we are uncertain. The level of resolution is important. A goal of simulation research using analogues such as the ISTD is that details (mechanisms) above the level of resolution will map to corresponding details *in vitro*. However, at a level of resolution, we can avoid making any claims about in silico-to-*in vitro* mappings. As the science progresses, a goal will be to replace simple objects that use rules and axioms (atomic components) with composite objects that reflect hypothesized mechanisms of interaction among lower scale components (finer-grained), where each of the finer-grained objects is atomic and uses rules and axioms as placeholders for even more detailed mechanisms. When the devices are properly designed, measurements taken from simulations of an ISTD having low-resolution components will be indistinguishable from measurements taken from simulations of another ISTD in which a set of low-resolution components have been replaced by higher-resolution components.

The enzyme component in Fig. 2 is an atomic component. Its behavior over multiple time steps was intended to mimic the corresponding behavior of two-site enzymes *in vitro* of the type described in the Appendix. The results in Table III and Figs. 7, 8, and 10 confirm that it does. However, the logic used by each enzyme (Fig. 3) within a simulation cycle is not intended to map to detailed events thought to occur (but not known for certain), even though posited details of those events guided design of the logic.

The simplest logic for controlling a compound's relocation to a particular, adjacent element is a simple probability

p: if PRN $\leq p$, then the object moves; otherwise, it remains within that element or does something else. However, we had no guidelines for selecting initial values for such probability parameters. Fortunately, we did have a rich literature of physical models describing expected compound behavior under idealized conditions. We elected initially to develop logics for compound movement using those physical models. In doing so, we have not changed ISTD resolution. We are uncertain about the details of events governing movement within each of the five spaces (more so, S2–4). We make no assumptions about actual events within *in vitro* counterparts of the 10^4 elements comprising each space. An element is the limit of spatial resolution. Nevertheless, the results show that the logic used, enabled the validation evidenced in Figs. 4 and 5.

Similarly, the logic used by a compound after entering a pore could have been based simply on a probability for exiting (in one direction or another) within a simulation cycle. However, because we had no prior parameterization guidelines, we again elected to base the logic on the accepted physical model (8) detailed in the Appendix. The logic is simply an in silico placeholder for uncertain events within uncertain tight junction environments. In this and the above situations, good science requires that multiple logic options be considered and evaluated against each other as this class of models evolves.

Experimenting with the ISTD

The feasibility (1,5,6,24) and scientific usefulness (25), (2) of synthetic, quantitative, discrete event models have been demonstrated. In this report, we began the iterative process of validation and refinement with the objective of taking an important step in achieving the five expectations stated in the Introduction. The simulation experiments were not designed to specifically demonstrate one of the nine capabilities in the Appendix, yet together they are evidence of important progress in achieving each. Collectively, the results demonstrate that for simulated passive trans- and paracellular transport of neutral, weak acid, and weak base compounds (MW $\leq$ 500), the ISTD functions acceptably as an in silico analogue of an *in vitro* TD without stirring. Because ISTD experimental results matched results from *in vitro* TD experiments closely, over a range of compounds and conditions, we can state that, viewed from the systemic perspective, the mechanisms driving in silico transport are a valid representation of those *in vitro*.

The data in Fig. 5b bring into focus differences between inductive models and ISTDs. We compared expected alfentanil transport from the two model types. The amount expected to be transported to the basal compartment was calculated using the mathematical model in (13); corresponding values were determined from the in silico experiments in Fig. 5a. Each trajectory in Fig. 5b is the ratio of these values. All trajectories approached 1.0 with increasing time. The largest deviations from 1.0 occur prior to 300 s. An exact match was not expected because the inductive, mathematical model and the ISTD are different. For example, the mathematical model assumes bulk flow and ignores the volume of cells. Consequently, there was no lag-time. Nor were there a following surge in drug appearance in the acceptor compartment. The ISTD did not use those assumptions. The simulations showed a short interval before compounds began reaching S5. During that interval, compounds accumulated in S3, and that caused a subsequent surge in compounds reaching S5. Such events are analogous to those observed *in vitro* at early times.

The results in Fig. 6 illustrate an advantage of this class of models. We tuned ISTD parameters to match the urea (Fig. 4) and then the alfentanil data (Fig. 5). Without further adjustments, we used the tuned ISTD to anticipate expected *in vitro* passive permeability properties of 14 other compounds known to undergo primarily passive transport. We did so by simply dosing the ISTD with each of 14 different compounds, labeled with compound-specific MW, pK_a, and logP_{ow} values, and then experimentally measuring the in silico permeability properties of each. No other information was used. The results in Fig. 6 matched reasonably well with the *in vitro* measures of transport for those drugs. It is noteworthy that expected values from a four-variable, linear model (Fig. 6) were no more accurate. Importantly, the permeability properties were essentially the same when the compounds were dosed together (Fig. 9). Having the capability of studying different compounds simultaneously provides a means of exploring drug–drug interactions in silico.

One might observe that an ISTD has many more parameters than the simple, four-variable linear model in Fig. 6 and thus express concern that the ISTD may be overparameterized. Actually, for Figs. 6 and 9, the ISTD uses just four parameters, the same PCP values used by the linear model. All other parameter values were fixed following the validations in Figs. 4 and 5.

Because the *in vitro* data in Fig. 6 came from different *in vitro* experiments, we cannot speculate on the origins of the discrepancies between simulated and *in vitro* values. For comparable data on several passively transported compounds, we anticipate iteratively refining the ISTD to simultaneously increase the similarity between simulated and *in vitro* logP_{eff} values for all compounds in the set. To do so, consideration of additional PCPs, including solubility, may be required. We may also need to simulate stirring in the donor compartment along with aspects of intracellular heterogeneity. For compounds subject to metabolism, the validated enzymes discussed below can be used. When multiple enzymes are implicated, separately specified sets of enzyme can be used. For compounds subject to one or more transporters, components similar to those used in (1) and (6) can be separately validated (as done here for enzymes), added, and then tuned along with the other system components.

The data in Figs. 7, 8, and 10 verify that in silico measures of compounds interacting with enzymes are consistent with what is expected, in theory, of drug molecules interacting with and being metabolized by enzymes having two interacting sites, even though the mapping between compounds and enzymes, and drug and enzyme molecules is not 1:1. The data in Fig. 8 provide validation evidence. Because the simulations only use S3, the results provide initial evidence of capabilities 5 (flexibility) and 6 (reusability). The data in Fig. 10 verify that identical enzymes interacting with two different compounds yield data consistent with what is expected for competitive inhibition in theory. Together, the results demonstrate that the operation-al properties of components intended for inclusion in the ISTD can be separately verified and validated using separately obtained *in vitro* data. Having such flexibility enables us to explore answers to questions such as this: if Caco-2 cells contained enzymes or transporters of a particular type, how might the *in vitro* permeability properties of a Caco-2 monolayer change for a compound known to be a substrate? The data in Figs. 9 and 10 demonstrate that the ISTD can be used to study multiple drugs simultaneously.

Interestingly, the verification studies (SM, Fig. S1) provided evidence that in the ISTD permeability declines for compounds having $\log P_{\mathrm{ow}} \geq 3$, especially for compounds having smaller MWs. These behaviors were emergent properties of the local mechanisms: they were not pre-specified.

Although we do not present specific examples of progress towards model adaptability (Appendix, capability 7), we have provided the necessary foundation for doing so. As a first step toward an in silico intestine, for example, it would be straight-forward to link several ISTDs in sequence and modify the merged S1 spaces to represent flowing intestinal content, and modify the merged S5 spaces to represent flowing blood.

In conclusion, we validated an ISTD as being a synthetic, discrete event analogue of Transwell devices. When given a dose of compound labeled with values of MW, pK_a, and $\log P_{\mathrm{ow}}$, the ISTD simulates the passive transport events that occur within Transwell devices. The results presented show that the measured in silico properties can stand as reasonable approximations of those expected from *in vitro* Transwell device studies of targeted compounds. The results also represent an important step forward in achieving simulation models that can help us better understand and anticipate the complex processes that underlie drug absorption and transport across cellular barriers, while providing a means for studying and exploring drug–drug interactions in silico.

ACKNOWLEDGMENT

This research was funded in part by grant R21CDH00101 from the CDH Research Foundation (of which CAH is a trustee). We thank Professors John Verboncoeur and George Sensabaugh for encouragement. We thank the members of Biosystems Group for helpful discussions, with special thanks going Teddy Lam, Sean Kim, Mark Grant, and Li Yan for commentary on the manuscript, to Sunwoo Park for technical support, and Glen Ropella for his support and keen technical and theoretical insights.

APPENDIX

Given the five expectations in the Introduction, we worked backwards and specified capabilities needed for their achievement, as done by Grant *et al.* (29), Tang *et al.* (30), and Hunt *et al.* (5) in other modeling contexts. It will require the design and validation of new types of in silico devices that can exhibit at least nine capabilities.

1. *Turing test*: In silico "transport" data are, to a domain expert (in a type of Turing test), experimentally indistinguishable from the referent wet-lab transport data; achieving this capability requires the in silico device to be suitable for experimentation.
2. *Phenotype overlap*: There is meaningful overlap between in silico and *in vitro* system phenotypes. Consequently, the events occurring during simulated transport, for example, accurately represent corresponding *in vitro* events at a level of detail (granularity) sufficient to mimic or predict specific phenotypic attributes. The concepts underlying designing analogues to achieve phenotype overlap (29,30) are similar to those on which Pattern-Oriented Modeling is based (31).
3. *Mappings*: Observables in silico are designed to be consistent with *in vitro* observables. Doing so enables clear mappings between *in vitro* and in silico components and mechanisms.
4. *Transparency*: Simulation details as they unfold need to be visualizable, measurable, and comparable where feasible to those of the *in vitro* system.
5. *Flexibility*: It must be relatively simple to increase or decrease detail in order to simulate an additional phenotypic attribute or change usage and assumptions, without requiring significant reengineering. Achieving this capability will enable cycles of scientific testing and device refinement, as new wet-lab data becomes available. Having flexible methods will lead to improved, more realistic and heuristic analogue systems.
6. *Reusability*: Device components can be designed to be autonomous and thus can be easily reconfigured to represent different cell types, experimental conditions, and compounds, *alone or in combination*. It must be easy to simulate and analyze outcomes of several different in silico experiments in a fraction of the time (and at a fraction of the cost) required to complete the wet-lab experiments.
7. *Adaptability*: In addition to flexibility and reusability, the components must be constructed so that they can be adapted to function as components in physiologically based, intestine and whole organism models.
8. *Components articulate*: Because the system attributes of interest may result from interactions of autonomous components, to study alternative mechanisms it must be easy to join, disconnect, and replace them without having to reengineer the in silico device or its components.
9. *Local mechanisms*: as *in vitro*, the behaviors that emerge during a simulation are the consequences of local mechanisms–local component interactions.

To enable these capabilities, the in silico device must be synthetic, as is the *in vitro* model (4,5), and its framework must use discrete interactions. Temporally and spatially discrete models offer theoretical and practical advantages because they allow, even facilitate achieving the preceding capabilities. Moreover, in the case where a continuous model is desirable, a discrete model can simulate or approximate it to arbitrary precision (25).

The equations to determine D (including D_a and D_m) are:

$$D = \varpi \frac{K_B T}{6\pi\eta r}, \quad \text{where} \quad r = \sqrt[3]{\frac{3V}{4\pi}} \quad \text{and} \quad V = \lambda . \cdot MW.$$

The first equation is the Stokes–Einstein equation to calculate the diffusion coefficient for Brownian spheres. K_B is the Boltzmans constant, ϖ is a remedy coefficient ($\varpi = 1$ for the cell membranes and 1.67 for aqueous spaces). η is the viscosity at 37°C, $\eta = 5e-3$ Pa s for membranes and $0.69e-3$ Pa s for aqueous spaces). r is the radius of the referent molecule assuming it is an ideal sphere and V is the molecular van der Waals volume. V is proportional to MW with $\lambda = 1.6755$ according to the data in (12).

The equations to determine D_{eff} in tight junctions are from (8) and (14):

$$D_{eff} = \frac{\varepsilon DF}{\tau}\left(f_0 + \sum_{\kappa} f_\kappa \left(\frac{\kappa}{1 - e^{-\kappa}}\right)\right), \text{ where } F = \left(1 - \frac{r}{R}\right)^2 \left(1 - 2.104\frac{r}{R} + 2.09\left(\frac{r}{R}\right)^3 - 0.95\left(\frac{r}{R}\right)^5\right), \text{ and } \kappa = {}^{ez|\Delta\psi|}/_{KT}$$

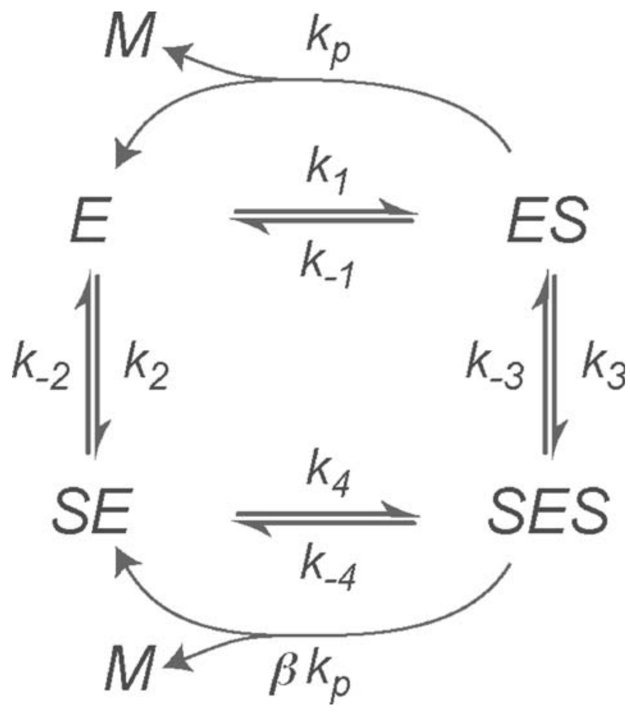

Fig. 11. A kinetic model for substrate inhibition from (17). When S binds to the catalytic site of the enzyme (ES), the rate and $V_{\max}$ of product formation (ES –> M) are determined by k_p[ES] and $k_p[E_{\text{total}}]$, respectively. When S binds to the inhibitory site (SE) that is non-productive, the rate of SES → M is determined by factor β ($0 \leq \beta \leq 1$). Dissociation constants for all species are defined by $K_S = k_{-1}/k_1$, $K_i = k_{-2}/k_2$, $\alpha' K_i = k_{-3}/k_3$ and $\alpha' K_S = k_{-4}/k_4$. All parameters are shown in Table III using the above equation.

D_{eff} is the effective diffusion coefficient through the tight junctions. ε is the proportion of surface area covered by the tight junctions. D is the aqueous diffusion coefficient. F is the Renkin factor to describe the sieving effect of tight junctions on molecules of different sizes. τ is the tortuousity of the tight junction passage, which is estimated as 2.5–3.0 times the height of tight junctions. κ is the electrochemical energy. f_0 is the fraction of unionized molecules and f_κ is the fraction of charged molecules. R is the estimated average tight junction pore size. e is the unit charge of an electron. z is the valence of a molecule. $\Delta\psi$ is the electrical potential difference across the membrane. K is the thermal constant, and T is the Kelvin temperature converted from 37°C.

The mathematical equations derived from (8) to compute P_{total} are:

$$\frac{M_R}{M_{D(0)}} = \left(\frac{H_R}{H_R + H_D}\right)\left(1 - e^{-\alpha\beta T}\right), \text{ where } \alpha = {}^{P_{total}}/_{H_D}, \text{ and } \beta = {}^{(H_R + H_D)}/_{H_R}$$

M_R is the mass in the acceptor space; $M_{D(0)}$ is the initial mass in the donor space; H_R (2.6/4.71 cm) and H_D (1.5/4.71 cm) are the thicknesses of the receiver and donor spaces, respectively; T is time.

The analytical solution to the substrate initial reaction rate v in the presence of inhibitors for the two-site enzyme is based on the kinetic model in Fig. 11, and is (17):

$$v = \frac{V_{\max}\left(\frac{1}{K_s} + \frac{\beta'[S]}{\alpha' K_i K_s}\right)}{\frac{1}{[S]} + \frac{1}{K_s} + \frac{1}{K_i} + \frac{[S]}{\alpha' K_i K_s}}$$

$V_{\max}$ is the maximal reaction rate of the substrate without inhibitors; K_S is the Michaelis–Menten constant of the substrate; K_i is the Michaelis–Menten constant of the inhibitor; α' is the enhancing factor for the second site binding when one and only one site is bound with a molecule; $\beta'(0 \leq \beta' \leq 1)$ is the inhibition factor of generating metabolites. The parameters in Table III used the equation above. Dissociation constants for all species in Fig. 11 are defined by $K_S = k_{-1}/k_1$, $K_i = k_{-2}/k_2$, $\alpha' K_i = k_{-3}/k_3$ and $\alpha' K_S = k_{-4}/k_4$.

REFERENCES

1. Y. Liu and C. A. Hunt. Studies of intestinal drug transport using an in silico epithelio-mimetic device. *Biosystems* **82**:154–167 (2005).
2. Y. Liu and C.A. Hunt. Mechanistic study of the cellular interplay of transport and metabolism using the synthetic modeling method. *Pharm. Res.* **23**:493–505 (2006).
3. G. E. Ropella, C. A. Hunt, and D. A. Nag. Using heuristic models to bridge the gap between analytic and experimental models in biology. In L. Yilmaz (ed), *Agent-Directed Simulation Symposium*, Vol. Simulation Series 37(2) (ADS'05). SCS Press, San Diego, CA, 2005, pp. 182–190.
4. G. E. P. Ropella, C. A. Hunt, and S. Sheikh-Bahaei. Methodological considerations of heuristic modeling of biological systems. *9th World Multi-Conference on Systemics, Cybernetics and Informatics*, Orlando, FL, 2005.

5. C. A. Hunt, G. E. Ropella, L. Yan, D. Y. Hung, and M. S. Roberts. Physiologically based synthetic models of hepatic disposition. *J. Pharmacokinet. Pharmacodyn.* **33**:737–772 (2006).
6. S. Sheikh-Bahaei and C. A. Hunt. Prediction of *in vitro* hepatic biliary excretion using stochastic agent-based modeling and fuzzy clustering. In: L. F. Perrone *et al*. (eds.), *Proc. of the 37th Conference on Winter Simulation,* 1617–24 (2006).
7. S. RailsbackAgent-based simulation platforms: review and development recommendations. *Simulation* **82**:609–623 (2006).
8. G. T. Knipp, N. F. Ho, C. L. Barsuhn, and R. T. Borchardt. Paracellular diffusion in Caco-2 cell monolayers: effect of perturbation on the transport of hydrophilic compounds that vary in charge and size. *J. Pharm. Sci.* **86**:1105–1110 (1997).
9. R. Hine. Membrane, *The Facts on File Dictionary of Biology*, Checkmark, New York, 1999, pp. 198.
10. P. Ball. Introduction to discrete event simulation, *2nd DYCOMANS workshop on "Management and Control: Tools in Action,"* Algarve, Portugal, 1996, pp. 367–76.
11. T. H. Cormen, C. E. LeisersonR. L. Rivest. *Introduction to algorithms*, McGraw-Hill, New York, 1990.
12. G. Camenisch, G. Folkers, and H. Waterbeemdvan de. Review of theoretical passive drug absorption models: historical background, recent developments and limitations. *Pharm. Acta Helv.* **71**:309–327 (1996).
13. K. Palm, K. Luthman, J. Ros, J. Grasjo, and P. Artursson. Effect of molecular charge on intestinal epithelial drug transport: pH-dependent transport of cationic drugs. *J. Pharmacol. Exp. Ther.* **291**:435–443 (1999).
14. K. Obata, K. Sugano, R. Saitoh, A. Higashida, Y. Nabuchi, M. Machida, and Y. Aso. Prediction of oral drug absorption in humans by theoretical passive absorption model. *Int. J. Pharm.* **293**:183–192 (2005).
15. S. Narasimhulu. Differential behavior of the sub-sites of cytochrome 450 active site in binding of substrates, and products (implications for coupling/uncoupling). *Biochim. Biophys. Acta* **1770**:360–375 (2007).
16. W. M. Atkins. Non-Michaelis–Menten kinetics in cytochrome P450-catalyzed reactions. *Annu. Rev. Pharmacol. Toxicol.* **45**:291–310 (2005).
17. M. Shou, Y. Lin, P. Lu, C. Tang, Q. Mei, D. Cui, W. Tang, J. S. Ngui, C. C. Lin, R. Singh, B. K. Wong, J. A. Yergey, J. H. Lin, P. G. Pearson, T. A. Baillie, A. D. Rodrigues, and T. H. Rushmore. Enzyme kinetics of cytochrome P450-mediated reactions. *Current Drug Metabolism* **2**:17–36 (2001).
18. K. R. Korzekwa, N. Krishnamachary, M. Shou, A. Ogai, R. A. Parise, A. E. Rettie, F. J. Gonzalez, and T. S. Tracy. Evaluation of atypical cytochrome P450 kinetics with two-substrate models: evidence that multiple substrates can simultaneously bind to cytochrome P450 active sites. *Biochemistry* **37**:4137–4147 (1998).
19. G. Camenisch, G. Folkers, and H. Waterbeemdvan de. Shapes of membrane permeability–lipophilicity curves: extension of theoretical models with an aqueous pore pathway. *Eur. J. Pharm. Sci.* **6**:325–329 (1998).
20. H. Lennernas. Does fluid flow across the intestinal mucosa affect quantitative oral drug absorption? Is it time for a reevaluation?. *Pharm. Res.* **12**:1573–1582 (1995).
21. P. Artursson, K. Palm, and K. Luthman. Caco-2 monolayers in experimental and theoretical predictions of drug transport. *Adv. Drug Deliv. Rev.* **46**:27–43 (2001).
22. Defense Modeling and Simulation Office, United States Department of Defense. *Online M&S Glossary*. https://www.dmso.mil/public/resources/glossary/, Cited 3/27/07. Part of the Defense Modeling and Simulation Office Web site, https://www.dmso.mil/public/, Cited 3/27/07.
23. A. Avdeef. Physicochemical profiling (solubility, permeability and charge state). *Curr. Top. Med. Chem.* **1**:277–351 (2001).
24. A. Barat, H. J. Ruskin, and M. Crane. Probabilistic models for drug dissolution. Part 1. Review of Monte Carlo and stochastic cellular automata approaches. *Simul. Model. Pract. Theory* **14**:843–856 (2006).
25. V. Grimm, E. Revilla, U. Berger, F. Jeltsch, W. M. Mooij, S. F. Railsback, H. H. Thulke, J. Weiner, T. Wiegand, and D. L. DeAngelis. Pattern-oriented modeling of agent-based complex systems: lessons from ecology. *Science* **310**:987–991 (2005).
26. B. Faller. Enhancing knowledge through combination of in-silico and *in-vitro* ADME profiling assays, 1st annual phys. chem. symposium: early ADME and medical chemistry, Obernai, France, (2004). http://www.acdlabs.com/download/publ/2004/eum04/adme.pdf/. Cited 3/27/07.
27. R. Schulz and D. Winne. Relationship between antipyrine absorption and blood flow rate in rat jejunum, ileum, and colon. *Naunyn–Schmiedeberg's Arch. Pharmacol.* **335**:97–102 (1987).
28. N. Mork, H Bundgaard, M Shalmi, S Christensen. Furosemide prodrugs: synthesis, enzymatic hydrolysis and solubility of various furosemide esters. *Int. J. Pharm.* **60**:163–169 (1990).
29. M. R. Grant, K. E. Mostov, T. D. Tlsty, and C. A. Hunt. Simulating properties of *in vitro* epithelial cell morphogenesis. *PLoS Comput. Biol.* **2**:e129 (2006).
30. J. Tang, K. F. Ley, and C. A. Hunt. Dynamics of in silico leukocyte rolling, activation, and adhesion. *BMC Syst. Biol.* **1**:14 (2007).
31. B. P. Zeigler, H. PraehoferT. G. Kim. *Theory of modeling and simulation: integrating discrete event and continuous complex dynamic systems*, Academic, San Diego, 2000.